

# THE USE OF COMPUTATIONAL FLUID DYNAMICS IN THE INVESTIGATION OF STALL ONSET ON TILT-ROTOR BLADES

Mark A. Woodgate, Thomas A. Fitzgibbon, and George N. Barakos

CFD Laboratory, School of Engineering, James Watt South Building, University of Glasgow, G12 8QQ, U.K.

Email: [mark.woodgate@glasgow.ac.uk](mailto:mark.woodgate@glasgow.ac.uk) [t.fitzgibbon.1@research.gla.ac.uk](mailto:t.fitzgibbon.1@research.gla.ac.uk)

[george.barakos@glasgow.ac.uk](mailto:george.barakos@glasgow.ac.uk)

## Abstract

An experimental setup has been designed to examine rotor blade stall flutter. The blade had to be designed so that it does not exceed the maximum permissible load on the rotor rig to be employed for wind tunnel tests, while maximising the blade loading to allow for the blade to be excited. An original set of blades were first tested to examine the possibility of their reuse. On discovery that they required too much power to drive them at the required collective computational fluid dynamics (CFD) was used to aid a new design.

## 1 INTRODUCTION

MENTOR (Methods and Experiments for NOvel Rotorcraft) is a project of the UKVLN (UK Vertical Lift Network). The aim of MENTOR is to develop and validate methods and tools that can be used for the design and analysis of the next-generation rotorcraft. As part of this goal a comprehensive study of rotor blade flutter will be carried out using both simulations and experiments in the University of Glasgow de Havilland wind tunnel. CFD is used to support the experiment, find the stall flutter boundary and design blades that can approach stall while their loads are within the limits of the employed rotor testing facility.

Examples of propeller flutter include classical bending-torsion flutter which is governed by the interaction between the out-of-phase bending motion and the torsional motion are excited via an external aerodynamic loading[1], and stall flutter that is defined as the oscillation of the body, due to partial or full separation of the flow field. Rotor blades are prone to working within the stall region due to the requirement of a large angle of attack on the retreating side of the rotor disk. A rotor blade experiencing separated flow shows loading fluctuations which can alter the pitching and bending, changing its shape. The interaction of the non-linear aerodynamics and the blade structure produces highly complex phenomena that cannot easily be modelled with low-fidelity methods. Hence methods that correctly capture the complex three-dimensional stalled flow and its interaction with the blade are required to accurately

estimate the stall flutter boundary which will allow for improved blade design and expansion of the flight envelope. [2]

## 2 CFD METHOD

All calculations were performed using the parallel CFD solver HMB3 (Helicopter Multi Block) [3]. HMB3 solves the dimensionless 3D Navier-Stokes equations in integral form using the Arbitrary Lagrangian Eulerian (ALE) formulation [4] for time-dependent domains with moving boundaries:

$$(1) \quad \frac{d}{dt} \int_{V(t)} W dV + \int_{\partial V(t)} [F_i(W) - F_v(W)] \cdot n dS = S$$

where  $V$  is the time dependent control volume,  $\partial V$  is the boundary of the control volume,  $W$  is the vector of conservative variables ( $\rho, \rho u, \rho v, \rho w, \rho E$ ),  $n$  is the unit vector on the boundary,  $F_i$  and  $F_v$  are the inviscid and viscous fluxes respectively.

The Navier-Stokes equations are discretized on the multi-block grid, using a cell-centered finite volume approach. A curvilinear coordinate system is adopted to simplify the formulation of the discretized terms, since body-conforming grids are adopted. The system of equations to be solved is:

$$(2) \quad \frac{d}{dt} [W_{i,j,k} V_{i,j,k}] + R_{i,j,k} = 0.$$

Copyright Statement© The authors confirm that they, and/or their company or organisation, hold copyright on all of the original material included in this paper. The authors also confirm that they have obtained permission, from the copyright holder of any third party material included in this paper, to publish it as part of their paper. The authors confirm that they give permission, or have obtained permission from the copyright holder of this paper, for the publication and distribution of this paper as part of the ERF proceedings or as individual offprints from the proceedings and for inclusion in a freely accessible web-based repository.

In the above  $W_{i,j,k}$  is the vector of conserved variables in the  $(i, j, k)$  cell,  $V_{i,j,k}$  denotes the volume of the cell and  $R_{i,j,k}$  represents the flux residual.

Osher's upwind scheme [5] is used to resolve the convective fluxes for its robustness, accuracy and stability properties. The Monotone Upstream-centered Schemes for Conservation Laws (MUSCL) [6] variable extrapolation method is employed in conjunction to formally provide second-order accuracy. The van Albada limiter [7] is also applied to remove any spurious oscillations across shock waves and near steep gradients. The integration in time is performed with an implicit dual-time method [8] to achieve fast convergence. The linear system is solved using a Krylov subspace algorithm, the generalised conjugate gradient method [9], with a block incomplete lower-upper (BILU) factorization as a pre-conditioner. The viscous stress tensor is approximated in HMB3 using the Boussinesq hypothesis. Several turbulence modelling options are available in HMB3 and for this work the  $k-\omega$  SST model is used [10].

## 2.1 CFD/CSD Coupling

There are a number of aero-elastic formulations in HMB3 and this work uses a "middleware" to directly couple HMB3 to MSC/Nastran. The middleware is the interface between HMB3 and MSC/Nastran and is responsible for the interpolation of the dynamic loading between the CFD blade surface mesh and the points when the loads are applied on the structural model and the interpolation of the displacements from MSC/Nastran to the CFD blade surface mesh. Figure 1 shows a schematic of the different types of data communication between HMB3 and MSC/Nastran.

The "middleware" allows for a variety of structural models and coupling methods without having to change the CFD solver.

## 3 Rotor Rig

The rotor rig is to be installed at the university of Glasgow de Havilland wind tunnel which is part of the UK national wind tunnel facility. It is a closed return tunnel with an octagonal working cross section 2.66m wide by 2.1m high and 5.4m long with a maximum speed of 70m/s. The power limits of the rotor rig are shown in table 1.

## 4 ORIGINAL BLADE DESIGN

This design became the initial point of the study with the dimensions of the blade shown in table 2 and the blade planform, aerofoil sections, and twist shown in figure 2. The blade shape was obtained using a second order polynomial to blend between sections. The blade sections were modified around the leading edges through

the addition and smoothing of control points and their trailing edge thickness was increased.

### 4.1 BLADE STRUCTURE

The structure of the blade can be seen in wire-frame representation in figure 3. The aerofoil skin was made from composite material of carbon epoxy resin and was approximately 1mm thick. To increase the stiffness of the aerofoil skin a composite D spar with a foam core was included. The root fitting was manufactured from aluminium to keep the weight down. Since the blades are removable a shear pin manufactured from maraging steel is used to connect the blades to the pitch shaft. To increase the root fitting in the area around the shear pin, collar rings of maraging steel were also included. Finally, the root tip is used as a balancing solution.

## 5 COMPUTATIONAL SETUP

The original blade design was targeting a rotor spinning at 2800 RPM resulting in a tip Mach number of 0.6 with an inflow velocity with 40m/s which equates to 0.194 of the tip velocity. This inflow velocity is relatively small compared to the tip velocity but is at the upper limit of what the wind tunnels can deliver. These conditions result in a tip Reynolds number of 1.06 million. The steady computation results were calculated using the axial flow formulation of HMB3 meaning that the flow is assumed to be periodic in both space and time. While the unsteady results were assumed only to be periodic in space, allowing for single blade calculations.

### 5.1 ORIGINAL BLADE DESIGN RESULTS

To examine whether the stall loads are within the specification of the rotor rig close to stall, first the collective of the Figure 5 shows the surface pressure coefficient of the original blade design at three different collectives. The blade appears to just be about to show a recirculation bubble at around 90% span. This region grew in width at 30° collective. In steady state calculations the recirculation bubble does not detach from the blade but it gives a reasonable estimate at what angle the blade is likely to stall at. Table 3 shows the force and moment data for the complete rotor at different collectives. While the thrust of the rotor was within the specifications of the rotor rig both the torque and power greatly exceeded the rig specification.

## 6 MODIFIED HIGH TWIST BLADE DESIGN

Initially, the first idea was to maintain original planform of the blade and so a high twist version of the original blade was also tested. The high twist blade (HTB)

was exactly the same as the original blade but with  $7^\circ$  of additional twist. This resulted in  $5.26^\circ$  more twist added to the root section and  $1.74^\circ$  of twist removed for the tip, with the  $70\%R$  at zero. The HTB was analysed with CFD at the same flow conditions as the original blade and the results are compared. Both steady axial flow, and single blade unsteady formulation were used. The unsteady formulations allows for the vortical flow features to detach from the blade. This comparison between hover and single bladed unsteady calculation highlighted any deficiencies in trying to determine the collective where stall occurs with a steady state formulation.

## 6.1 COMPUTATIONAL RESULTS

Figure 6 shows the pressure coefficient for the high twist blade design which can be compared against the original blade shown in Figure 5. The two blades produce very similar surface pressure coefficient plots. The formulation of the stall region at around  $90\%$  of the blade span is delayed slightly for the high twist blade. This is because the collective angle is measured at  $70\%R$  of the blade span meaning the out-board region of the high twisted blade has a lower angle of attack as  $1.74^\circ$  twist was removed from the tip.

Figure 7 shows the comparison between the surface pressures of the high twist blade at three different collectives comparing the steady and unsteady results. The unsteady formulation started with a collective of  $24^\circ$  and the ramp up in blade collective commenced after half a revolution and continued through  $10^\circ$  during next half a revolution. This resulted in a final collective of  $34^\circ$  which was maintained for another two revolutions. The pressure coefficient plots show very similar results and this confirms that using the steady formulation is valid for approximating the collective at which stall occurs.

Figure 8 shows the comparisons of the thrust and torque between the steady original blade and high twist blade as well as the high twist unsteady computation. The steady and unsteady results show a similar trend. The large change in rate of collective will delay the stall until after  $34^\circ$ . Figure 9(a) shows the surface pressure coefficient around a rotor cycle after the maximum collective has been reached while figure 9(b) shows the vortical structures behind the blade using the Q-criterion. Both figures highlight that the separation extends much farther inboard than the steady and its not just a single flow feature.

## 7 FINAL BLADE DESIGN

The initial blade designs have tried to maintain the original blade platform with a blade radius of  $700\text{mm}$  and a blade tip chord of  $74\text{mm}$ . It was been shown that although the thrust was within specification of the rotor rig the torque and power were not. The techniques of

reducing the thickness of the sections, and increasing the blade twist had little effect on the torque. The on-coming air flow was also reduced to one fifth of the blade tip speed and to reduce it any lower to reduce the collective angle where stall occurs at, resulted in an unrealistic forward velocity for a tilt rotor blades.

The inclusion of stall devices was undesirable. This resulted in only two options for reducing the torque. Firstly to change the aerofoil shapes and secondly to change the blade planform. Since there is a cost implication of re-designing and manufacturing of the blade root with original fittings, which were already designed to work with the rotor rig that part of the blade would be recycled and hence the option of reducing both the blade radius and tip chord was explored to reduce the torque. However, it should be noted that the requirement of a large aerodynamic loading, to be able to excite the structure, is accomplished when the blade is as large as possible and so the torque will be close to rotor rig design specification.

The new design reused the root fitting so the blade is unchanged up to  $266.1\text{mm}$  as shown in figure 10. Table 5 shows that over half the components have been reused from the original design.

The changes from the original blade are as follows:-

- The blade tip chord has been reduced to  $60\text{mm}$  and, is a linear variation from the end of the root fitting until the tip. This results in nearly  $20\%$  reduction in the size of the blade tip chord compared to the original blade.
- The blade tip thickness is now  $6\text{mm}$  (the Vertol V23010\_1.58 is  $10\%$  thick aerofoil), down from  $7.5\text{mm}$  for the original blade. This is the minimum thickness required for the manufacturing of the blade.
- The trailing edge now has a constant thickness of  $0.47\text{mm}$  which was taken from the thickness at the end the fitting from the original blade. The trailing edge of the original blade reduced in thickness slightly towards the tip.
- The blade radius was reduced from  $700\text{mm}$  to  $625\text{mm}$ . This is the cause for most of the reduction in torque of the blade and allows it to come within the limits of the rotor rig.
- The tip cap has a constant  $60\text{mm}$  chord it is  $10\text{mm}$  wide and has no twist.
- The twist variation has been calculated using blade element theory assuming an inflow of  $40\text{m/s}$  and a tip velocity of  $205\text{m/s}$ .

### 7.1 MSC/NASTRAN MODEL

The generated CAD model was used in the construction of the unstructured finite element mesh shown in figure 11. Each component was generated separately using a mixture of element types. The components

were connected via two different methods. The surfaces that co-inside on the skin, D spar and foam fillers were perfectly matching and were connected by merging the nodes on these surfaces to construct the volume mesh with a set of unique mesh points. However, this is not possible to achieve this with the triangular surface mesh associated with the root fitting and the quadrilateral mesh associated with blade skin. These components were connected through the MSC/Nastran support of permanent glued contact. The segment-to-segment contact region was used because it tends to produce a more continuous distribution of stresses across the discontinuous glued interface compared to the node-to-segment method. Each component was added to a three-dimensional deformable contact body and these were connected together through the definition of a contact pair with geometric and physical contact parameters which describe the type of contact involved. Single point constraints were also used on the root of the fitting to clamp the root of the blade for modal analysis.

## 7.2 COMPUTATIONAL RESULTS

The test conditions for the short blade were slightly different from the 700mm radius cases. Due to the reduction in radius, the resulting tip speed for a given RPM was also reduced. Hence the RPM of the blade was increased to 3000 RPM that is the maximum permitted by the rotor rig. This rotational velocity resulted in a tip speed of 196m/s which was about 5% lower than the original calculations. The inflow velocity was also reduced to 38m/s to keep the ratio of the tip speed to the inflow velocity the same in both cases. The lower tip speed also resulted in a lower tip Reynolds number of 0.864 Million.

Figure 12 shows the surface pressure coefficient at six different collectives. A recirculation bubble starts to form when the collective reaches  $31^\circ$ . By the time the collective is at  $34^\circ$  the flow has a very large recirculation region.

Figure 13 shows the cross-section pressure coefficient through the recirculation bubble, scaled with the local wind velocity, at 88.4% and 93.4% span for a range of collective values. At both stations as the collective increases the suction peak strengthens and stall occurs, signified by the pressure coefficient at the trailing edge decreasing causing a fairly constant pressure coefficient over the final 70% of the chord. This effect occurs at  $32^\circ$  collective at the inboard station and a degree later at the outboard station as the separation bubble expands in the spanwise direction. This indicates that the onset of stall is at around  $32^\circ$  of collective.

Table 6 shows the different thrust, torque and power requirements for the different collective values. At  $32^\circ$  degrees of collective both the thrust and torque are well within their specs of the rotor rig while the power requirements are about 10% too high. This will be okay in practise since the motor on the rotor rig is rated at

140kW and a deliverable power of 80kW is conservative for a direct drive system when taking losses into account.

Figure 14 shows the start of the separation bubble at  $31^\circ$  collective and the expanded bubble at  $33^\circ$ , as well as, a well defined tip vortex. There is a large recirculating flow region on the upper surface of the blade signifying the blade is likely to have already stalled.

Finally, figure 15 shows the deformation of the blade at  $30^\circ$  collective. The blade tip deflects up to 52.9mm and has a small amount of blade torsion where the tip is rotated nose down by  $0.5^\circ$  degrees.

## 8 CONCLUSIONS AND FUTURE WORK

The newly designed short blade has a torque at the onset of stall about 285Nm down from around 450Nm for the original blade, and is within specification. This is likely to be an over-estimate since finer grids calculations normally reduce both the thrust and torque of the blade from a coarse mesh CFD simulation. Also the calculations used the Reynolds averaged Navier stokes (RANS) and Menter's shear stress transport turbulence model that also delays the onset of stall compared to a more realistic unsteady SST-SAS (Menter's shear stress transport with scale-adaptive simulation) turbulence model. This model uses unsteady Reynolds average Navier-Stokes (URANS) with large eddy simulation (LES) type content in the unsteady regions and produces less eddy viscosity away from the solid walls.

Future work includes numerical computations, with the wind tunnel modelled to examine the blockage effects, and dynamic simulations to examine the behaviour of the blade as it spins up and transitions to the correct conditions without damaging the blade or its stops on the rotor hub.

## 9 Acknowledgments

This work is funded by MENtOR (EP/S013814/1). The work also used the Cirrus UK National Tier-2 HPC Service at EPCC (<http://www.cirrus.ac.uk>) under project ec004 and the ARCHER UK National Supercomputing Service (<http://www.archer.ac.uk>) under project e613.

## 10 REFERENCES

### References

- [1] Wright, J. R. and Cooper, J. E., *Introduction to aircraft aeroelasticity and loads*, John Wiley & Sons, 2nd ed., 2015.

- [2] Higgins, R. J., Jimenez-Garcia, A., Barakos, G. N., and Bown, N., "High-fidelity computational fluid dynamics methods for the simulation of propeller stall flutter," *AIAA Journal*, Vol. 57, No. 12, 2019, pp. 5281–5292.
- [3] Steijl, R., Barakos, G., and Badcock, K., "A framework for CFD analysis of helicopter rotors in hover and forward flight," *International Journal for Numerical Methods in Fluids*, Vol. 51, No. 8, 2006, pp. 819–847.
- [4] Hirt, C., Amsden, A., and Cook, J., "An arbitrary Lagrangian-Eulerian computing method for all flow speeds," *Journal of Computational Physics*, Vol. 14, No. 3, 1974, pp. 227 – 253.
- [5] Osher, S. and Chakravarthy, S., "Upwind schemes and boundary conditions with applications to Euler equations in general geometries," *Journal of Computational Physics*, Vol. 50, No. 3, 1983, pp. 447–481.
- [6] van Leer, B., "Towards the ultimate conservative difference scheme. V. A second-order sequel to Godunov's method," *Journal of Computational Physics*, Vol. 32, No. 1, 1979, pp. 101–136.
- [7] Van Albada, G., Van Leer, B., and Roberts Jr, W., "A comparative study of computational methods in cosmic gas dynamics," *Astronomy and Astrophysics*, Vol. 108, 1982, pp. 76–84.
- [8] Jameson, A., "Time Dependent Calculations Using Multigrid, with Applications to Unsteady Flows Past Airfoils and Wings," *10<sup>th</sup> Computational Fluid Dynamics Conference*, Honolulu, HI, 24-26 June 1991, AIAA-1991-1596.
- [9] Eisenstat, S. C., Elman, H. C., and Schultz, M. H., "Variational Iterative Methods for Nonsymmetric Systems of Linear Equations," *SIAM Journal on Numerical Analysis*, Vol. 20, No. 2, 1983, pp. 345–357.
- [10] Menter, F., "Two-Equation Eddy-Viscosity Turbulence Models for Engineering Applications," *AIAA Journal*, Vol. 32, No. 8, 1993, pp. 1598–1605.

## 11 TABLES AND FIGURES

	Thrust	Torque	Power
Maximum	3.4kW	350Nm	80kW

Table 1: Thrust, torque and power limits of the rotor rig.

Parameter		Parameter		Section	Name
Rotor radius	700mm	Cone angle	0°	Y=190mm	NACA 64-128
Root chord	84.2mm	Tip chord	73.7mm	Y=400mm	Vertol V43015.2.48
Inboard cut-off	186mm	Trailing Edge thickness	0.35mm	Y=690mm	Vertol V23010.1.58

Table 2: Characteristics and dimensions of the original model scale blade design.

Collective	Thrust (N)	Power (kW)	Torque (Nm)
24	1318	73.8	251
26	1561	90.6	308
28	1776	107.3	365
30	1909	121.8	415
32	1976	134.8	458

Table 3: The thrust, torque and power requirements vs. collective for the original blade design.

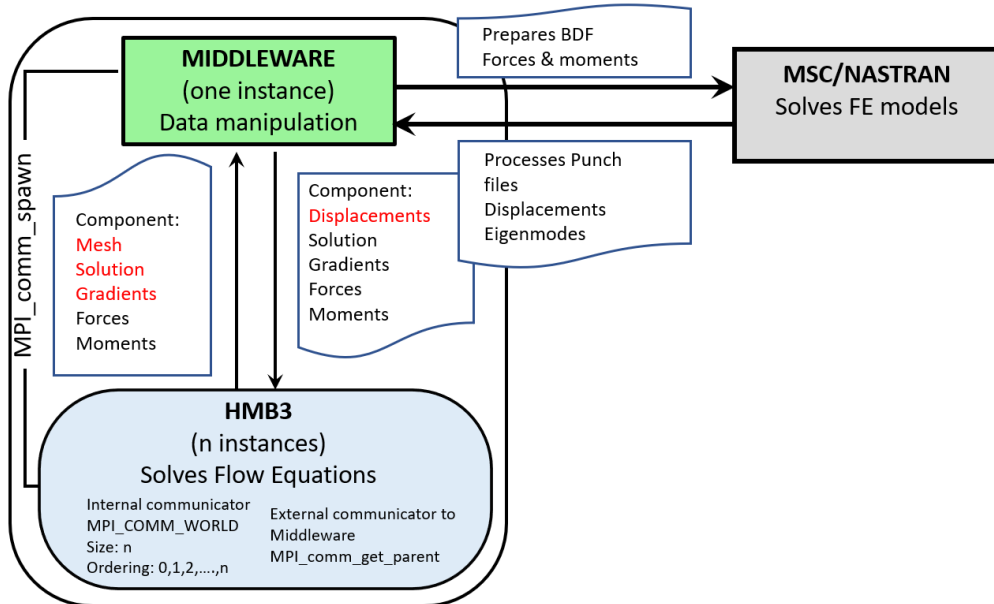


Figure 1: Schematic of the different types of data communication allowed in the middleware.

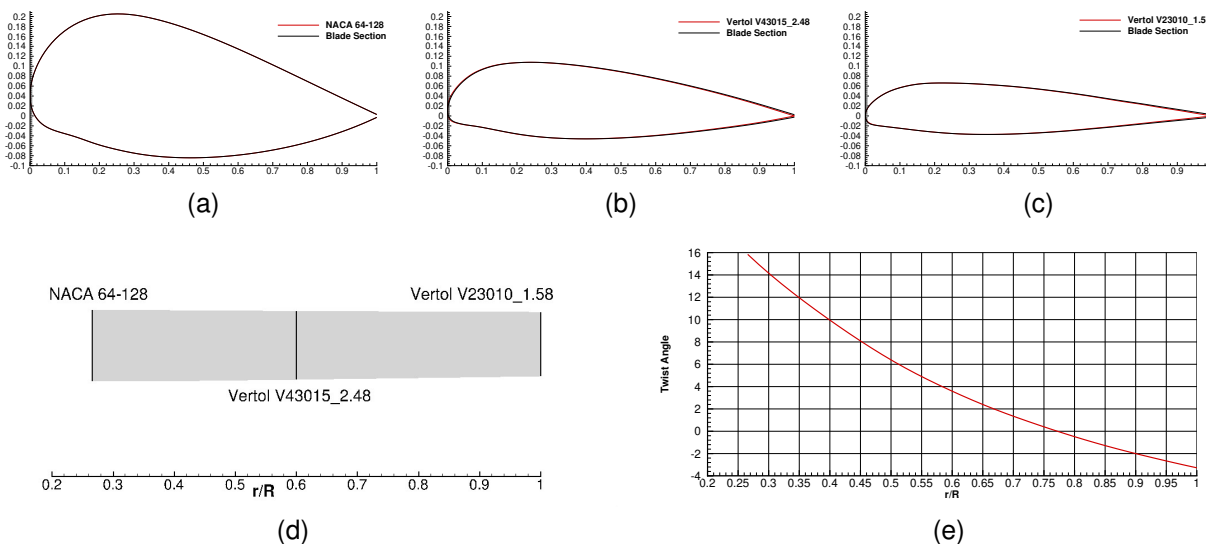


Figure 2: Schematic of the original blade design.

Collective	Original Blade			High Twist Blade			High Twist Blade (Uns)		
	T (N)	P (kW)	$\tau$ (Nm)	T (N)	P (kW)	$\tau$ (Nm)	T (N)	P (kW)	$\tau$ (Nm)
24	1318	73.8	251	1229	71.9	245	1379	74.3	253
26	1561	90.6	308	1542	88.1	299	1638	93.0	316
28	1776	107.3	365	1767	105.0	357	1887	111.2	378
30	1909	121.8	415	1942	120.7	411	2084	128.5	437
32	1976	134.8	458	N/A	N/A	N/A	2191	146.6	499
34	N/A	N/A	N/A	N/A	N/A	N/A	2185	157.1	534

Table 4: The thrust, torque and power requirements vs. collective for the original and high twist blade design.

Part	DS5836-1	Fitting	Pin	Ring		Spar		Tip Cap	Blade Skin
				Down	Up	Foam	Shell		
Modified	No	No	No	No	No	Yes	Yes	Yes	Yes

Table 5: Changes to the structural model for the short blade.

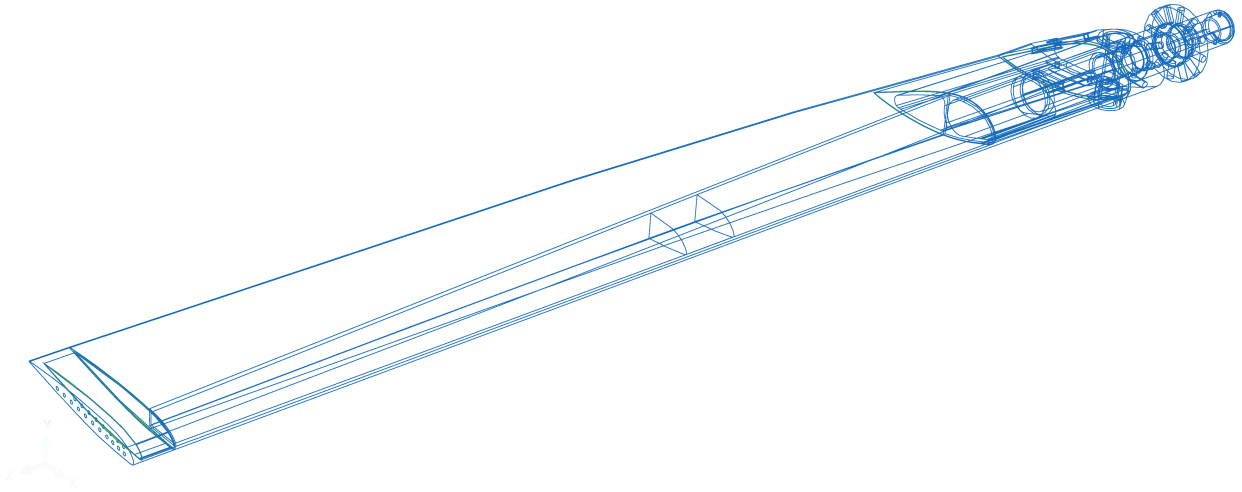


Figure 3: Schematic of the original blade design structural model. Wire frame diagram of the the complete tilt rotor blade (Aerofoil skin, D-spar, root fitting, shear pin, collar rings, and pitch shaft.)

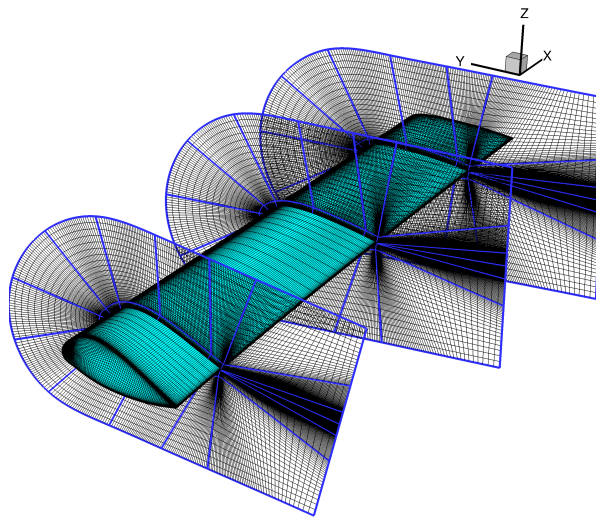


Figure 4: Original blade design with CFD volume mesh

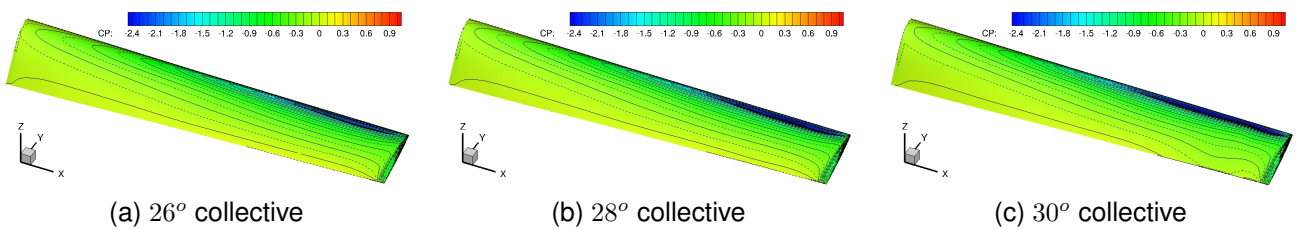


Figure 5: Surface pressure co-efficient for the original blade design at different collectives.

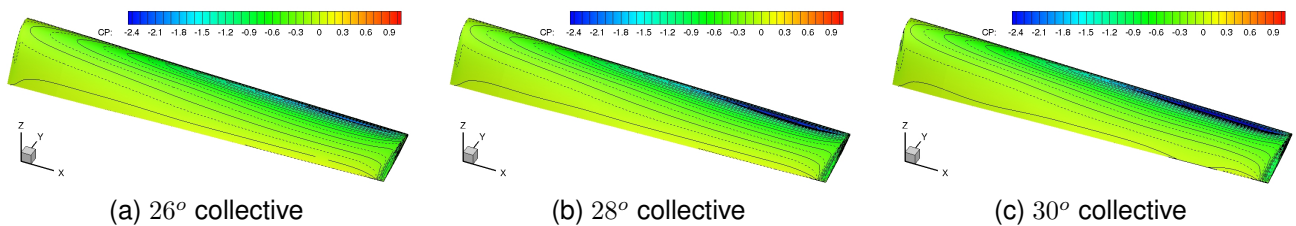


Figure 6: Surface pressure co-efficient for the high twist blade design at different collectives.

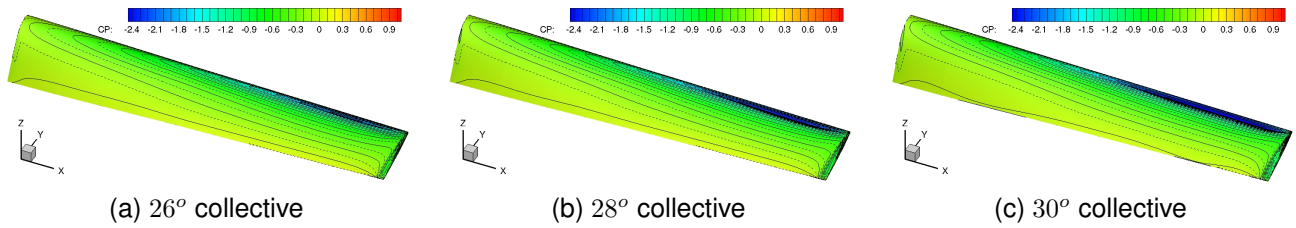


Figure 7: Surface pressure co-efficient for the high twist blade design at different collectives obtained using unsteady aerodynamics.

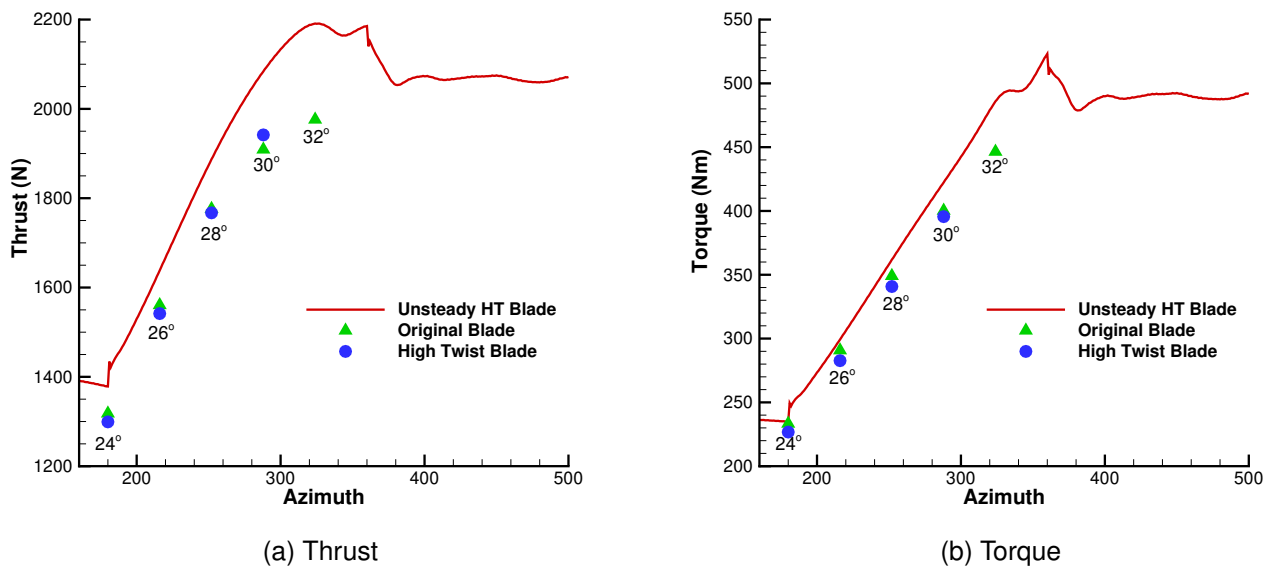
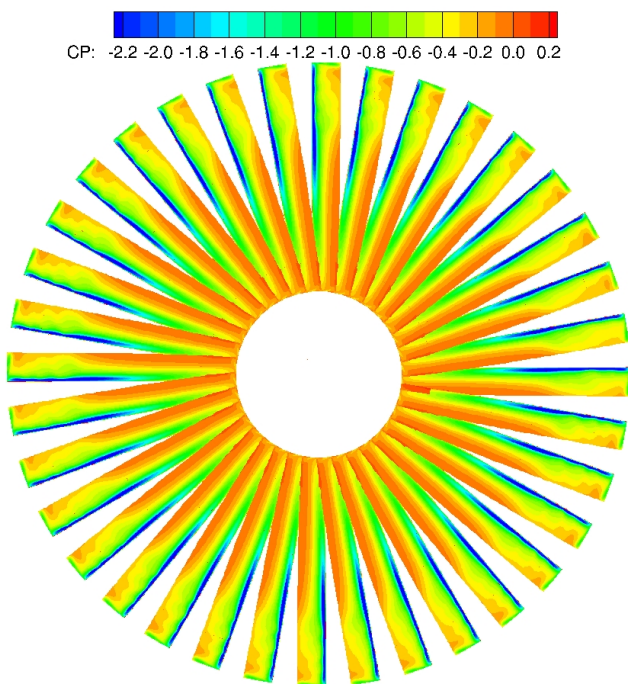


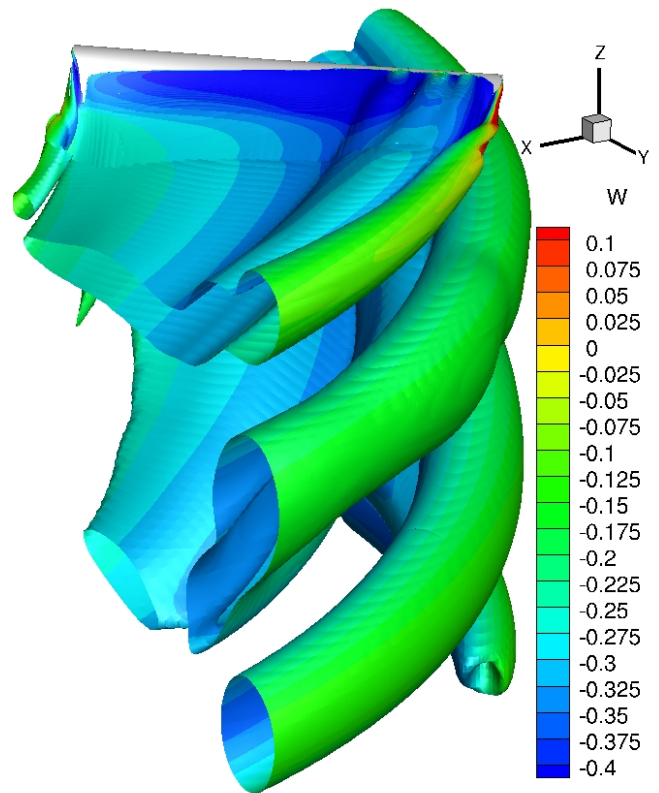
Figure 8: Comparison of thrust and torque on different blades at different collective angles

Collective Angle	Short Blade		
	Thrust N	Torque Nm	Power (kW)
25.0°	737	149	46.8
27.0°	1119	199	62.4
29.0°	1277	236	73.9
30.0°	1345	253	79.5
31.0°	1401	270	84.7
32.0°	1426	285	89.3
33.0°	1453	299	93.8
34.0°	1468	313	98.1
35.0°	1486	328	102.9
36.0°	1499	344	108.1

Table 6: Total thrust torque and power for the short blade at different collective angles



(a) Variation in surface pressure coefficient



(b) Vortical structure behind the blade

Figure 9: Surface pressure coefficient for the second revolution and Vortical structure using unsteady aerodynamics

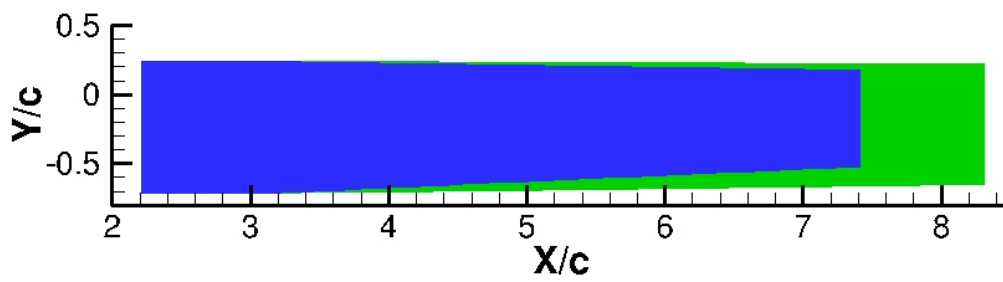


Figure 10: Planform of the original Blade (Green) and the short blade (blue) scaled with the root chord.

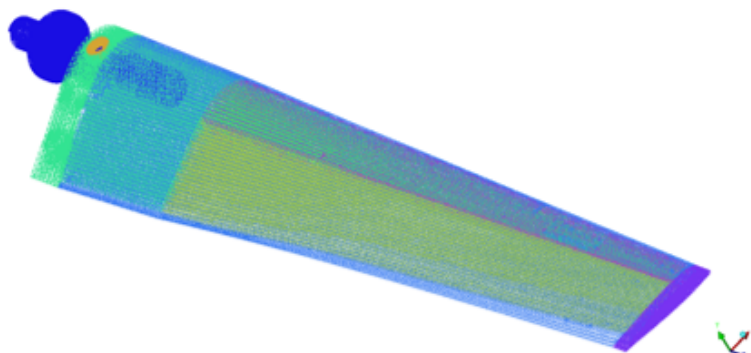


Figure 11: MSC/Nastran structural mesh for the short blade.

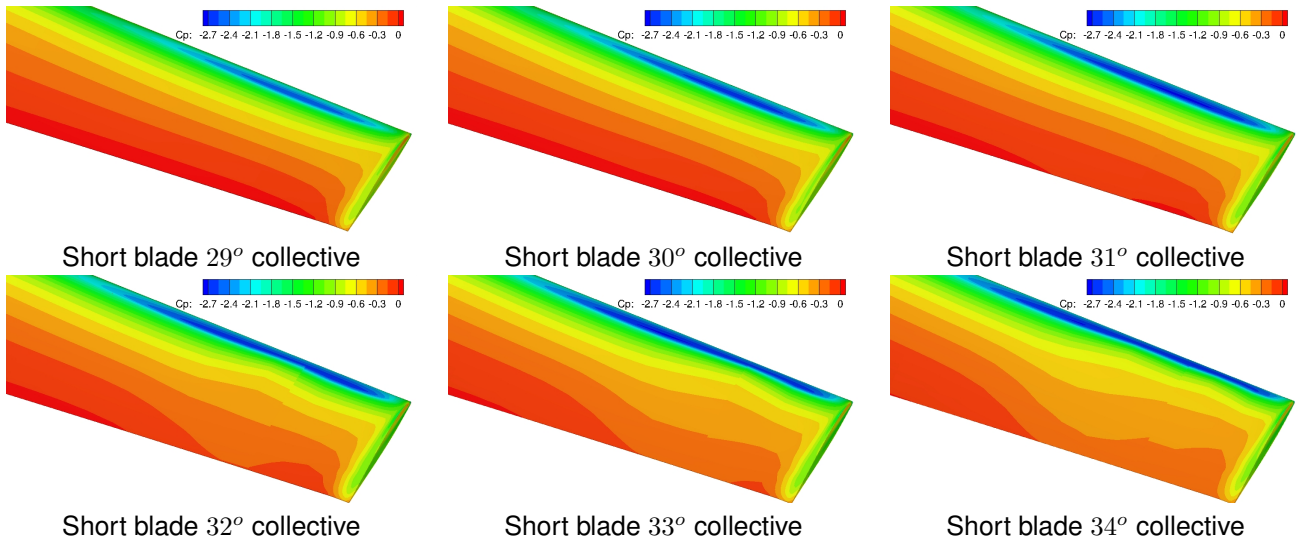


Figure 12: Pressure coefficient for the short blade spinning at 3000 RPM with an inflow velocity 38m/s and tip Reynolds number of 0.864 million at six different collectives.

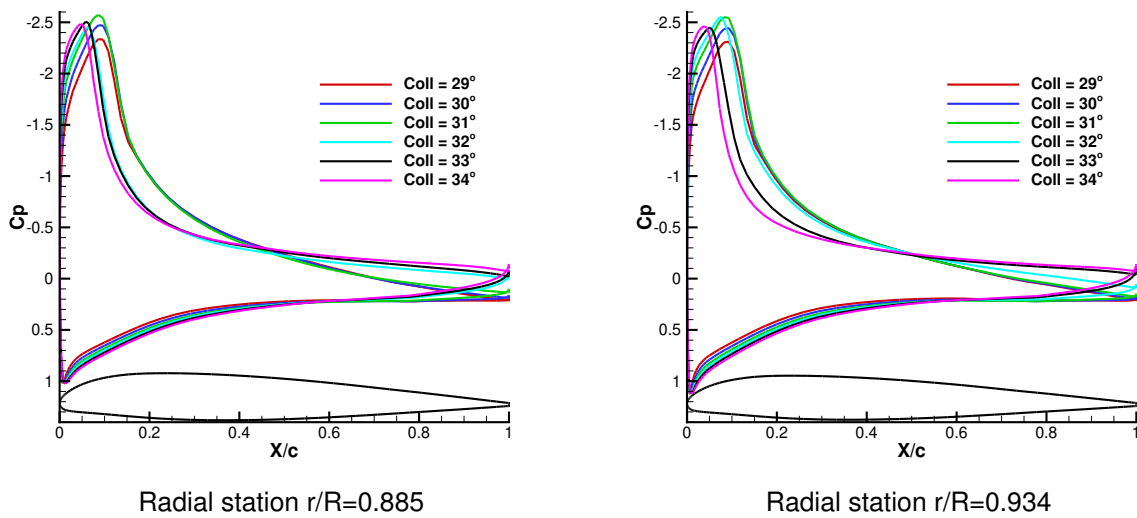


Figure 13: Comparison of sectional pressure coefficient at two different stations along the blade at different collective angles.

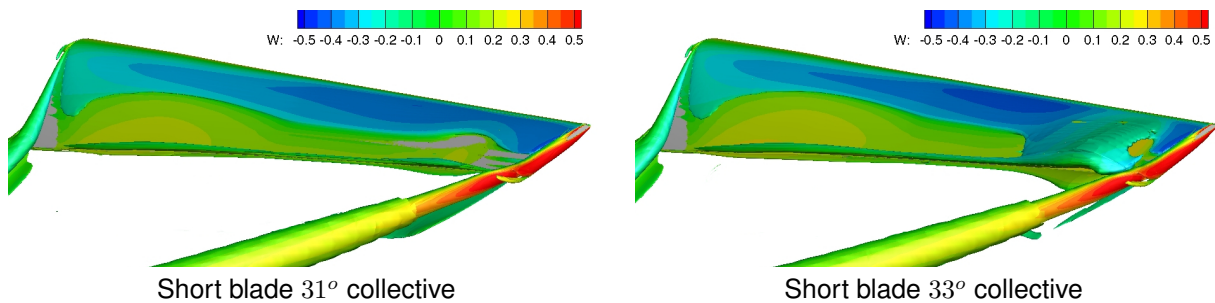


Figure 14: Comparison of the size of the separation bubble for the short blade spinning at 3000 RPM with an inflow velocity 38m/s and tip Reynolds number of 0.864 million at two different collectives.

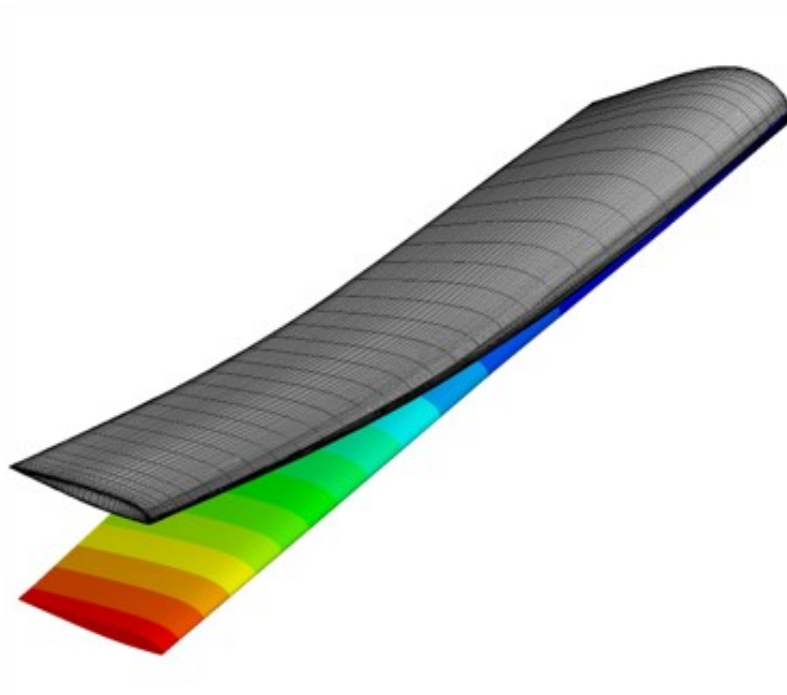


Figure 15: The deflection of the short blade under aerodynamic loading at  $31^\circ$  Collective.